Solution-Processed Synthesis of Nano-Sized Argyrodite Solid Electrolytes with Cavitation Effect for High Performance All-Solid-State Lithium-Ion Batteries

Youngjun Huh+,[a, b] Hae Gon Lee+,[a] Chang-Min Cho,[a] Jun-Woo Park,[a] Byung Gon Kim,[a] You-Jin Lee,[a] Heetaek Park,[a] Yoon-Cheol Ha,[a] Jeong-Hee Choi,[a] Jeongdoo Yi,[c] Sang-Min Lee,*[a, d] Je In Lee,*[b] and Jun-Ho Park*[a]

To mitigate poor contact issues between electrolyte/electrode materials interfaces of all-solid-state batteries (ASSB), we newly introduce a novel solution-processed synthesis that exploits the differences in the boiling point and polarity of the two solvents (i.e., methanol, and toluene), with a cavitation effect by bubbling inert gas. Through this process, called solvent exchange with bubbles (SEB), the Li_6PS_5Cl solid electrolyte is synthesized with a particle size below 800 nm and sufficient ionic conductivity of 1.54 mS/cm at 25 °C. In addition, the ASSB cell consisting of the cathode electrode with Li_6PS_5Cl synthesized by the SEB exhibited a high capacity of 176 mAh/g at 0.1 C (55 °C) owing to the improved contact between the electrode and solid electrolyte. In particular, the rate capability of the cell is superior to that of a cell with Li_6PS_5Cl prepared by ball milling.

Introduction

Owing to the ever-increasing demand for batteries with increasing energy and power densities, extensive technological research has been conducted to improve the performance of lithium-ion batteries (LIBs).[1–3] However, LIBs with organic liquid electrolytes still present safety concerns owing to their flammable characteristics and the possibility of liquid electrolyte leakage. To prevent such accidents, all-solid-state lithium batteries (ASSLBs) have recently received significant attention as potentially safe and stable high-energy storage systems. A relatively stable solid-state electrolyte can offer higher energy density, better safety, longer cycle life, and a wider operating temperature range than the flammable and toxic liquid electrolytes of commercial LIBs.[4,5]

In recent years, many studies have been conducted to improve the mechanisms and performance of various solid electrolytes such as sulfide-based,[3,6–9] nitride-based,[10–12] halide-based[13–15] and oxide-based electrolytes.[16–18] Among these, sulfide-based solid electrolytes, in particular, Li_6PS_5Cl, are known to exhibit higher ionic conductivity than oxide-based solid electrolytes because of the better polarization of S^{2-} compared to O^{2-}.[19] These electrolytes exhibit a high conductivity of 10^{-3} S/cm at room temperature. In addition, sulfide-based solid electrolytes exhibit good deformability even under low external stress,[20] low side reactivity with lithium cathodes,[21–23] and relatively low synthesis temperatures compared to oxides and phosphates.

Despite the aforementioned advantages of solid electrolytes that distinguish them from liquid electrolytes, problems hindering the practical use of ASSLBs still remain. A central challenge is to construct effective ionic conduction pathways throughout the entire ASSLBs cell. In particular, the high interfacial resistance at the electrolyte/electrode interface is a fundamental obstacle in the formation of an effective ion-conducting network. According to previous studies, this interfacial resistance mainly originates from poor solid-solid contact at the electrolyte/electrode interface.[24–28] It comes from coarse grain size similarity of solid electrolyte and active material. Therefore, the electrolyte/electrode interface is a critical factor for achieving excellent performance in ASSLB cells

[a] Y. Huh,+ Dr. H. Gon Lee,+ Dr. C.-M. Cho, Dr. J.-W. Park, Dr. B. Gon Kim, Dr. Y.-J. Lee, Dr. H. Park, Dr. Y.-C. Ha, Dr. J.-H. Choi, Dr. S.-M. Lee, Dr. J.-H. Park
Next Generation Battery Research Center,
Korea Electrotechnology Research Institute (KERI)
Changwon, Gyeongsangnam-do 51543 (Republic of Korea)
E-mail: sangma@postech.ac.kr
        junhopark@keri.re.kr
[b] Y. Huh,+ Prof. J. In Lee
School of Materials Science and Engineering,
Pusan National University
Busan 46241 (Republic of Korea)
E-mail: jilee@pnu.ac.kr
[c] J. Yi
SDI R&D Center,
Samsung SDI
130, Samsung-ro, Yeongtong-gu,
Suwon-si, Gyeonggi-do 16678 (Republic of Korea)
[d] Dr. S.-M. Lee
Graduate Institute of Ferrous and Energy Materials Technology,
Pohang University of Science and Technology (POSTECH)
77 Cheongam-Ro, Nam-gu, Pohang, Gyeongbuk 37673 (Republic of Korea)
[+] These authors contributed equally to this work.

with high ionic conductivity. However, the current perspective of researchers regarding the construction of effective ion-conducting networks within ASSLBs seems to remain limited.

A review of previous studies on solid electrolytes dedicated to all-solid-state batteries[29–33] shows that most studies have focused on improving the ionic conductivity of solid electrolytes through compositional changes or doping of the solid electrolyte. Conversely, there have been few attempts to improve cell performance by increasing the contact area between solid electrolytes and cathodes. Shi et al.[34] reported that reducing the particle size of the solid electrolyte mixed with the cathode can improve cell performance. From this study, it can be inferred that this critical but less addressed approach enables the formation of an effective ion-conducting network in ASSLBs by allowing intimate contact at the electrolyte/electrode interfaces. Consequently, small-sized particles entail dense and homogenous interfacial areas.

Thus, synthesizing sulfide solid electrolytes with finer morphologies is essential to accelerate the commercialization of ASSLBs. However, the majority of conventional sulfide-based solid electrolyte synthesis methods generally yield inhomogeneous and relatively large-sized active materials. Currently, the most widely used methods for preparing sulfide-based solid electrolytes, especially Li_6PS_5Cl, are mechanical milling and solution-based wet synthesis methods. Mechanical milling generally involves homogeneously mixing the precursor by milling a stoichiometric mixture of raw materials with chemically stabilized balls at a high rotation speed for several days to obtain the final material Li_6PS_5Cl. However, this synthesis method requires a high rotational speed and long milling times; moreover, it is low yielding, resulting in energy and time wastage. In particular, obtaining reproducible homogeneous materials is difficult owing to the high-speed milling process involved in this synthesis route.[22,35,36]

Conversely, solution-based wet synthesis methods using an organic solvent have recently been employed in many studies, because of the many advantages in terms of processing time and scale compared with the mechanical milling method. In particular, there are two representative solution-processed synthesis methods. One is a suspension method, in which a precursor is dispersed in an organic solvent, and after drying to remove the organic solvent, the resulting powder is annealed to obtain Li_6PS_5Cl with an argyrodite crystal structure.[37–39] The other method is the dissolution-precipitation method. The ready-made Li_6PS_5Cl solid electrolyte is dissolved in highly soluble organic solvents, such as hydrazine, methanol, and ethanol. The solvent is then removed by evaporation, leaving a solid product.[24,28] This method is widely used for infiltration or direct coating of active materials on the cathode electrode as a solid electrolyte solution state.[40,41] The particle size of Li_6PS_5Cl prepared by these wet synthesis methods is approximately 3 μm, which is fine compared to conventional mechanical milling. However, this is still comparable to that of the positive electrode material; finer submicron particles are required to form excellent interfacial contact between the positive electrode and active material.[24]

Therefore, herein, we introduce a novel synthetic process that can effectively refine the Li_6PS_5Cl particle size. In previous studies, we found that the boiling point and polarity of the solvent are important factors for controlling the particle size.[42,43] Based on the results of these previous studies, in this study, a solution-processed synthesis method, called the solvent exchange with bubble (SEB) method, was designed using the difference in boiling point and polarity of two solvents, with the cavitation bubbling effect. In this method, organic solvents with different roles, namely, the initial and final solvents, which have different boiling points and relative polarities, were selected. The former served to dissolve the solid electrolyte, and the latter served to independently precipitate the solid electrolyte particles from the solution. In addition, to prevent secondary particle agglomeration and to introduce the cavitation effect, the microdroplets of the solvents were refined, and the reaction temperature of the solid electrolyte-dissolving-solution was controlled.

Consequently, it was possible to obtain a submicron-sized solid electrolyte. We then maximized the cell performance by effectively controlling the particle size using this method. This new process is a simple and effective approach for controlling the particle size and effectively lowering the interfacial resistance at the electrolyte/electrode interfaces. The size-controllable solid electrolyte that maintained the argyrodite structure exhibited satisfactory lithium ion conductivity at 25 °C (1.54 mS/cm). Through electrochemical evaluation and electrode cross-section analysis, we also confirmed the excellent contact area between the $Li[Ni_{0.6}Co_{0.2}Mn_{0.2}]O_2$ (NCM 622) positive electrode material and solid electrolyte, which improved the cell performance. In addition, when the solid electrolyte prepared by our new synthesis method was introduced into a cell, an excellent discharge capacity of 176 mAh/g was obtained compared to that of the coarse solid electrolyte obtained by ball milling. The results of this study suggest a research and development direction for manufacturing solid electrolytes with excellent performance.

Results and Discussion

Design of solvent exchange synthesis process

As confirmed by the SEM images in Figure S1, the particle size of the layered cathode structure used in this study was approximately 13 μm in diameter. In addition, the size of the cathode material was comparable to that of sulfide-based solid electrolyte particles synthesized by simple dry ball milling. The similarity in their sizes induces the formation of poor solid-solid contact, leading to a high interfacial resistance at the electrolyte/electrode interfaces. An exceptionally fine solid electrolyte, with a particle size of 1 μm or less is required to facilitate the smooth movement of lithium ions through intimate surface contact.[44] However, when a solid electrolyte particle is prepared via simple dry ball milling, large-sized effective particles are generally obtained because secondary aggregation

Batteries & Supercaps

Research Article
doi.org/10.1002/batt.202300036

Chemistry Europe
European Chemical
Societies Publishing

particles are formed between the sulfide-based solid electrolyte particles.

Therefore, in this study an effective particle size refinement was attempted by introducing a solution exchange synthesis process for the coarse-sized solid electrolyte obtained through simple ball milling. As shown in Figure 1, two organic solvents with different roles were employed: a highly polar solvent with a low boiling point and a low-polar solvent with a high boiling point, which are referred to as the initial solvent and final solvent, respectively. The initial solvent serves to dissolve the solid electrolyte to form the solid electrolyte solution, and the final solvent serves to precipitate the dissolved solid electrolyte solution, preventing agglomeration. As the initial solvent, it is important to select one that can completely dissolve the coarse solid electrolyte without unwanted side reactions. The solubility properties and SEM morphology images of the selected organic solvent candidates that serve as the initial solvent are shown in Figures S2 and S3, respectively. In Figure S2, the transparency properties when the solid electrolyte was dissolved in these organic solvents were compared using optical photography to observe their dissolution characteristics. Consistent results were observed according to the relative polarity of the organic solvent or type of functional group. In all the experimental groups, the organic solvent with a hydroxyl group was the most transparent. The solid electrolyte was best dissolved in an organic solvent having MeOH (methanol) rather than EtOH (ethanol) in the hydroxyl group. On the other hand, it was not dissolved in ACN (acetonitrile), Acetone, THF (tetrahydrofuran), Heptane, and Toluene, and existed in a suspension state, showing an opaque solution state. Thus, it can be observed that the dissolution ability of the solid electrolyte is related to the relative polarity of the organic solvent.

In contrast, the SEM images in Figure S3 were obtained by precipitating solid electrolyte particles dispersed in the initial organic solvents via the D&P method. From this result, the extent to which the particle size distribution of the Li_6PS_5Cl solid electrolyte is affected by the initial organic solvent selection was observed. Among the various organic solvents, a solvent with a hydroxyl group was found to be the most effective for controlling particle size. In other words, the solid electrolyte tends to have better solubility in a solvent having a relatively high polarity, and thus is effective in reducing the particle size. However, even in methanol solvents with high polarity, particles with sizes of several tens of micrometers are still observed, as shown in Figure S3. These large particles were attributed to the secondary agglomeration of primary particles during the solvent drying process.

Thus, novel synthetic processes, called the SE and SEB methods, were introduced in this study. For these methods, toluene was selected as a suitable final solvent with a lower solubility and a higher boiling point than that of the initial solvent. Unlike the D&P method, these solvent-exchange methods can effectively suppress the formation of large secondary particles by exploiting the differences in the thermal and electronic properties of the two solvents. The detailed mechanisms of these size reduction processes and the reasons for selecting two solvents with different properties for the solvent exchange method are detailed in the next section. Additionally, to prevent particle entanglements, the cavitation effect was introduced in the SEB method by refining the microdroplets into a solid-electrolyte-dissolving solution. This process was confirmed to be successful in synthesizing finer morphologies of the sulfide solid electrolyte, resulting in dense and intimate interfacial contact at the electrolyte/electrode interfaces.
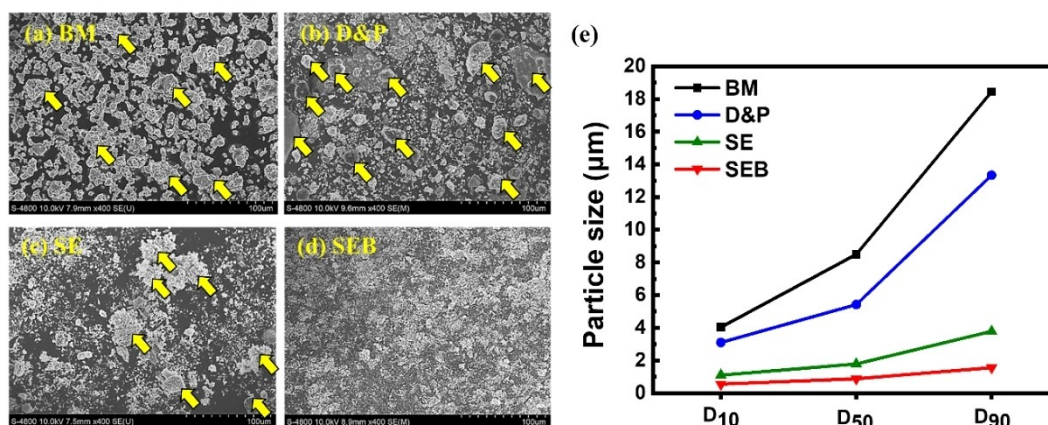
Li_6PS_5Cl solid electrolyte characterization

SEM images of the solid electrolytes according to different synthesis methods, such as BM, D&P, SE, and SEB, are shown in Figure 2(a–d). In addition, FE-SEM images and the detailed particle size distribution analysis results of the Li_6PS_5Cl particles are presented in Figure S5. In general, the particle size distribution of the Li_6PS_5Cl synthesized powder is non-uniform, and large particles are generated because the agglomeration rate is not constant in all directions during synthesis.[45] Therefore, large particles with a size of several tens of micrometers, indicated by yellow arrows in Figure 2(a–c), were easily observed in the BM, D&P, and SE methods.

In the SEM images in Figure 2(a, b), no clear difference was observed between the D&P and BM methods. Furthermore, the particle size distribution analysis in Figure S5 shows that the average particle diameter of the D&P method was ca. 5–6 μm, which is comparable to that of the BM method. This can be explained as follows. In the case of the D&P method, when Li_6PS_5Cl powder is added to a solvent with high polarity, a high surface charge is formed by the polar solvent on the solid electrolyte surface, creating a strong electric double layer. This layer helps the solid electrolyte to be well-dispersed in the initial solvent via the repulsive force between them.[46] However, when the first solvent is evaporated during the subsequent drying process, this electric double layer fades away, resulting in large secondary particle agglomeration
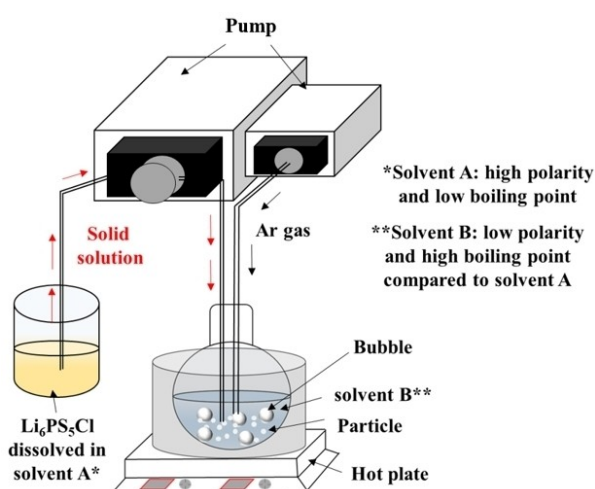
Figure 1. Schematic diagram of the Li_6PS_5Cl synthesis device using the solvent exchange with bubble (SEB) method.

Labels in figure:
Pump
*Solvent A: high polarity and low boiling point
**Solvent B: low polarity and high boiling point compared to solvent A
Solid solution
Ar gas
Bubble
solvent B**
Particle
Hot plate
Li_6PS_5Cl dissolved in solvent A*

Figure 2. FE-SEM images of Li_6PS_5Cl prepared by a) ball milling (BM), b) dissolution-precipitation (D&P), c) solvent exchange (SE), and d) solvent exchange with bubble (SEB). e) Particle size measurements results for each sample using SEM images.
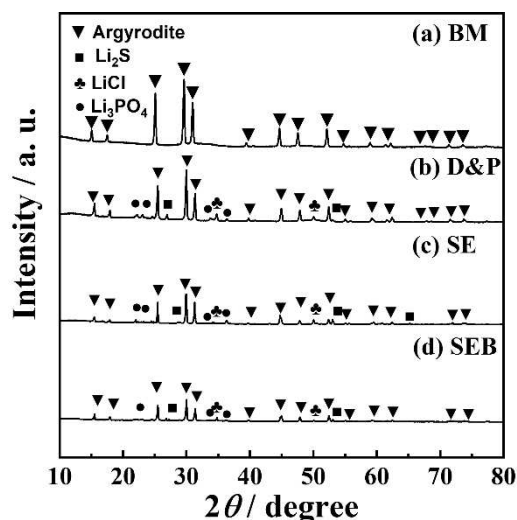
among these solution-dissolved solid electrolytes. Moreover, according to the results of Zhang et al., lower pH results in smaller particle sizes.[47] However, the initial solvent used in this study (i.e., methanol) is known to have high pH. Thus, it is suggested that the particle size cannot be effectively reduced in the D&P method compared to that in the BM method.[46]

Conversely, SEM images of solid electrolytes synthesized by the SE and SEB methods, are shown in Figure 2(c,d). This indicates that the particle size was relatively decreased by the solvent exchange methods compared to the conventional BM and D&P methods. The size reduction mechanism of the solvent exchange method can be explained as follows. As shown in Figure 1, when the solid electrolyte-dissolving solution is added to the final solvent that has reached a temperature above the boiling point of the initial solvent, the initial solvent quickly volatilizes during the dropping. The solvent then consisted of only the solid electrolyte dispersed in the final solvent with low polarity. A solvent with a low dipole moment has poor solubility in the solid electrolyte, thus helping the solid electrolyte to be independently precipitated while maintaining an exceptionally fine primary particle size. Accordingly, the final solvent of the SE and SEB methods can prevent primary particle agglomeration into micro-sized secondary particles, unlike in the D&P method. However, entangled particles between these precipitated primary particles are still observable even with the SE method, as indicated by the yellow arrows in Figure 2(c). However, these particles are different from the large agglomeration particles of the BM and D&P methods, as shown in Figure 2(a,b). This is because they are weakly intertwisted primary particles and do not have a large mass of secondary particles. This is evident from the particle distribution analysis shown in Figures 2(e) and S5. It can be seen that the distribution of D90, which is a large secondary particle, sharply decreases in SE compared with that in the BM and D&P methods. In addition, the average particle diameter of the SE method was ca. 1–2 μm which is significantly lower than that of the D&P method.

To prevent these entangled primary particles observed in the SE method, additional attempts were made to blow inert Ar

gas bubbles into the final solvent in the novel SEB method. From the results shown in Figure 2(e), it is confirmed that these weakly intertwisted primary particles of SE were completely resolved by applying gas bubbles to the solid electrolyte-dissolving solution. Furthermore, as shown in Figure S5, the average particle diameter of the SEB method (∼800 nm) was improved even more than that of the SE method. The shape of the primary particles reduced by the SEB method could be well confirmed in the magnified FE-SEM images in Figure S4. In this regard, it is presumed that this particle size reduction can be attributed to the cavitation energy generated by bubbling. However, the specific role and mechanism of the SEB bubbling process in reducing the size of Li_6PS_5Cl remains unclear. For a clear understanding, computational modeling results will be presented in the next section, along with the size reduction mechanism of the SEB method, which is inaccessible in the experiment. Consequently, the obtained particle size of SEB was the finest compared to that obtained by the BM, D&P, and SE methods. Thus, we expected this particle size to show the best electrochemical performance due to the intimate contact between the active material and the electrolyte.

Several analyses were conducted to analyze the crystal structure and chemical impurities of the obtained solid electrolyte powder, including XRD diffraction, Raman. From the XRD patterns in Figure 3(a–d), it can be seen that the argyrodite structure (F$\bar{4}$3 m) was mainly developed for all samples.[20,48] In the case of BM in Figure 3(a), almost no impurity phase peaks were observed. Based on the strong intensity of the argyrodite phase, it is considered that the crystalline phase was well-developed compared to the other samples. In the case of D&P in Figure 3(b), unreacted impurities, such as Li_3PO_4, Li_2S, and LiCl, were also observed. It is expected that during the MeOH solvent drying process, Li_3PO_4 was first generated by the residual MeOH component that was non-uniformly trapped in some agglomerated particles, and impurities such as Li_2S and LiCl were additionally generated because of the non-uniform composition. The XRD peak intensity was in the order BM > D&P > SE > SEB, and the intensity of Li_6PS_5Cl by SEB in Figure 3(d) was the lowest. In Figure 2(e), the progressively

Batteries & Supercaps

Research Article
doi.org/10.1002/batt.202300036

Chemistry Europe
European Chemical
Societies Publishing

Figure 3. XRD patterns of Li_6PS_5Cl prepared by a) solvent exchange with bubble (SEB), b) solvent exchange (SE), c) dissolution-precipitation (D&P), and d) ball milling (BM).

Table 1. Lithium ion conductivity and activation energy of each sample; BM(ball milling), D&P(dissolution-precipitation), SE(solvent exchange) and SEB(solvent exchange with bubble).
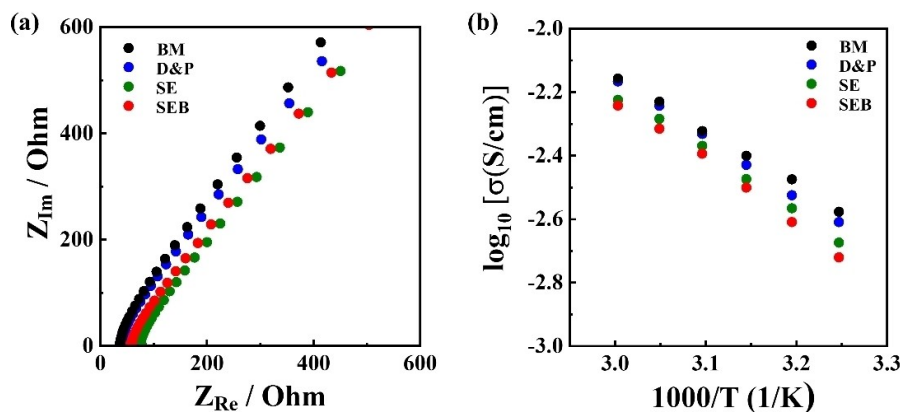
	Li ion conductivity/ mS cm^{-1}	Activation energy/ eV
BM method	1.74	0.339
D&P method	1.65	0.368
SE method	1.60	0.373
SEB method	1.54	0.394

structural stress of the Li_6PS_5Cl particles by the solvent exchange and bubbling process.

To evaluate the electrical characteristics of the obtained solid electrolyte powders, AC impedance spectra of the Li_6PS_5Cl solid electrolytes of the BM, D&P, SE, and SEB samples are compared in Figure 4(a) using SUS│Li_6PS_5Cl│SUS cells. Despite the synthesis by solution-processed methods, the impedance spectra of all synthesized Li_6PS_5Cl solid electrolytes did not exhibit a semicircle. This was because of the significantly low amount of residual organic solvents on the surface of Li_6PS_5Cl, resulting in decreased grain boundary resistance.[54] As can be seen from Table 1, the ionic conductivities of Li_6PS_5Cl solid electrolytes from the BM, D&P, SE, and SEB methods were 1.74 mS/cm, 1.65 mS/cm, 1.60 mS/cm, and 1.54 mS/cm, respectively. As the boundary resistance was low in Figure 4(a), the bulk resistance is expected to contribute a larger proportion of the total resistance than the boundary resistance, and such bulk resistance could depend on the crystallinity of the particles. Therefore, the lowest ionic conductivity of Li_6PS_5Cl fabricated by SEB is probably due to its lower crystallinity, which is attributed to its smaller particle size and these findings have been reported previously.[55–58] The activation energy was calculated using the Arrhenius equation:[59]

$$\sigma = A \exp(-E_a/kT)$$

As shown in Table 1, the activation energies of the Li_6PS_5Cl solid electrolytes prepared by the BM, D&P, SE, and SEB methods were 0.339, 0.368, 0.373, and 0.394 eV, respectively. From this result, it was found that the activation energy

decreasing particle size and the trend of decreasing intensity in XRD are identical. It was suggested that the cavitation energy generated by the bubbles caused intense physical stresses, followed by a reduction in the crystallite size.[49,50]

The coordination of the chemical species in the sample was further analyzed using the Raman spectra in Figure S6(a–d). A Raman peak centered at ca. 420 cm^{-1}, originating from the PS_4^{3-} unit, was detected in the bulk, indicating that the argyrodite structure was maintained.[36,51,52] In the case of SEB, SE, and D&P, as shown in Figure S6(a–c), the PS_4^{3-} units were solvated with hydroxyl groups, and the peak positions were shifted compared to BM (Figure S6d), as reported in a previous study.[53] In contrast, the Raman peaks of Li_6PS_5Cl prepared using SEB and SE in Figure S6(a,b) are in the same position as the D&P sample in Figure S6(c), indicating that the PS_4^{3-} unit was not affected by toluene. Among the obtained samples, Li_6PS_5Cl manufactured by SEB exhibited the lowest peak intensity. This is considered to be due to the increased

Figure 4. a) Impedance spectra of pelletized Li_6PS_5Cl prepared by each process and b) Arrhenius plots of each sample.

Batteries & Supercaps

Research Article
doi.org/10.1002/batt.202300036

Chemistry Europe
European Chemical
Societies Publishing

increased with decreasing particle crystallinity. As the crystallinity decreases, more defects and dislocations are created at the grain boundaries; the lithium ions require more energy to move between the grain boundaries.[60,61] Although the Li_6PS_5Cl fabricated by SEB has an ionic conductivity 10% lower than that of Li_6PS_5Cl prepared by the BM method, it has sufficiently high ionic conductivity (1.54 mS/cm) and a small particle size (ca. 800 nm); therefore, it is expected that the capacity of the all-solid-state battery prepared by the SEB method will be improved by widening the contact area between the active materials and the solid electrolyte.
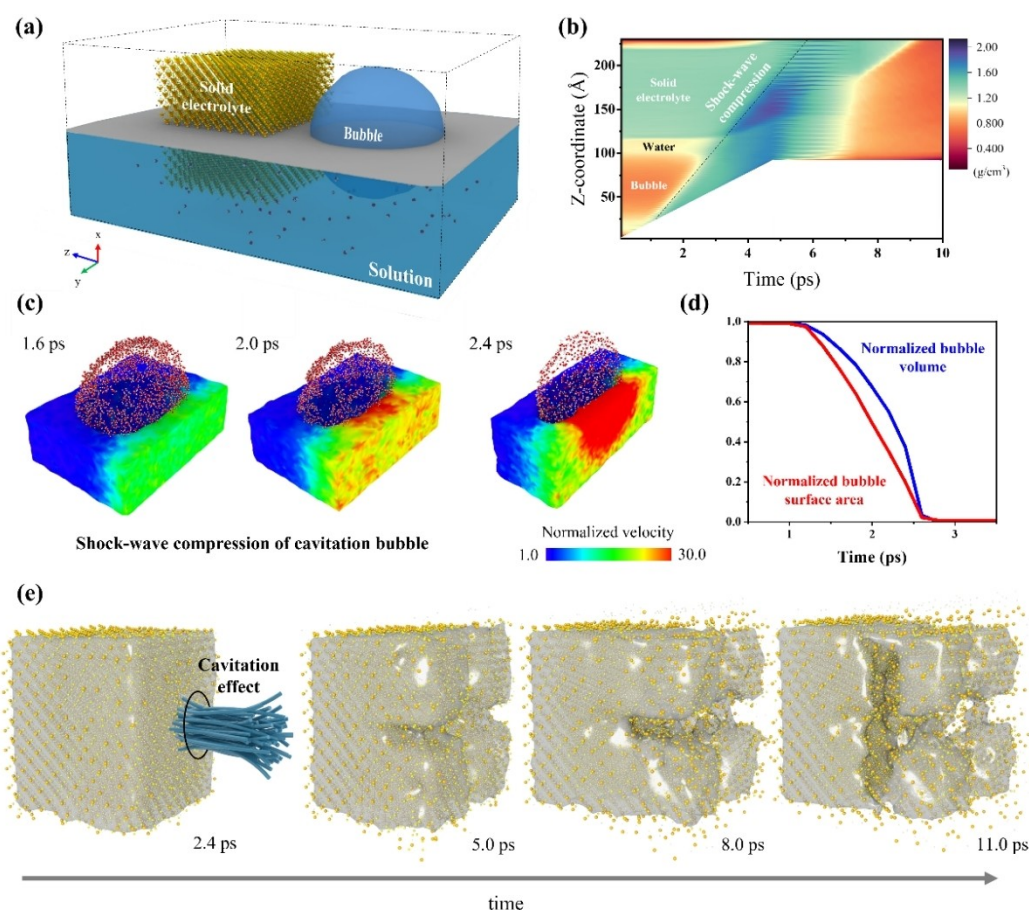
Shock-induced cavitation bubble collapse dynamics

From the aforementioned results, it is considered that bubbling dynamics play an important role in reducing the Li_6PS_5Cl particle size while maintaining their argyrodite structure. However, the detailed role and mechanism of the SEB bubbling process in Li_6PS_5Cl size reduction cannot be ascertained from these experimental results alone. The damage dynamics due to bubble collapse occur over short periods and small length scales and are thus difficult to observe through experimental methods. Therefore, MD simulations were performed to confirm whether the shock wave and jets generated during the process of bubble collapse lead to cavitation damage on the surface of the materials.

Generally, cavitation is defined by bubbles that are generated when the pressure falls below the saturated vapor pressure. In principle, cavitation bubbles are inherently unstable. That is, as soon as the pressure is reinstated above the vapor pressure by the external shock, they immediately collapse either inside the liquid or on the liquid-solid interface.[62] This external shock typically originates from chaotic chain dynamics within an unstable and uncontrollable solvation environment. When this shock wave interacts with bubbles in the vicinity of the surface, the cavitation bubbles collapse and a high-energy fluid jet is created, impacting the surface with a greater force than the front region of the impact. In particular, these surficial forces tend to become predominant at microscopic scales rather than at the macroscale, implying that bubbles collapsing near the tiny Li_6PS_5Cl surface can play a pivotal role in their size reduction during the SEB method.

To verify these dynamics, the response of the argyrodite particle to a high-speed fluid jet created by bubble collapse was investigated and is presented in Figure 5. As shown in

Figure 5. MD simulation results on solid electrolyte dynamics in response to shock-induced cavitation bubble collapse. a) Initial configuration of the cavitation bubble collapse simulation, b) contour plot of local density as a function of the simulation time and the z-coordinate, c) shape evolution of the bubble and normalized liquid molecule velocities around the bubble during collapse due to the shock wave at time $t = 1.6, 2.0, 2.4$ ps, d) changes in the surface area and volume as a function of time while the bubble is collapsing. e) Time snapshots of solid electrolyte collapse by impact of high-energy jet and vortex.

Batteries & Supercaps

Research Article
doi.org/10.1002/batt.202300036

Chemistry
Europe

European Chemical
Societies Publishing

Figure 5(a), the system consisted of a pure lithium argyrodite crystal (Li$_7$PS$_6$) suspended in a water solvent containing a similar-sized cavitation bubble. To initiate a chain of events, a planar shock along the z direction just outside the simulation box was generated using a momentum mirror method.[63] This method involves moving a massive piston to impact the solution during a noticeably short piston stop time of τ_s. After τ_s the piston stopped, but the shock wave continually propagated along the solid electrolyte dissolution solution. Subsequently, the shock wave causes the cavitation bubble to collapse near the crystal surface, creating a high-speed jet that can damage substances. For the case shown in Figure 5, bubbles diameter, piston velocity, piston stop time, and the offset distance between the bubble surface and the nearest solid electrolyte surface were set to $D = 9.0$ nm, $u_p = 2.0$ km/s, $\tau_s = 5.0$ ps, and $l = 2.0$ nm, respectively.

This series of phenomena can be closely observed in a time-dependent density plot, as shown in Figure 5(b). It shows the time-dependent average density plot along the z direction, which is parallel to the plane where a planar shock is produced. Initially, the density of z coordinate where the water and solid electrolyte are located were ca. 0.98 g/cm^3 and 1.35 g/cm^3, respectively. Because the solid electrolyte is immersed in the solution in the x and y directions, the density is computed to be lower than the theoretical values of the pure lithium argyrodite crystal (1.81 g/cm^3).[64] Under the impact of the shock wave, the shock front, represented by the dotted black line in the figure, continued to propagate.

Because the bubble did not have sufficient surface tension to restore and balance the shock wave compression, the bubble contracted, as shown in Figure 5(c). The time sequence of the changes in the bubble shape and size is presented. The shape of the proximal side of the bubble changed from spherical to elliptical; detailed information regarding the surface area and volume changes during the compression process is provided in Figure 5(d). At the onset of the bubble collapse at 1.6 ps, a sudden increase in the velocity of the solvent surrounding the bubble is observed in the normalized velocity plot of Figure 5(c). This was because the shock front reached the bottom of the bubble. A high-energy fluid jet is then created across the low-density void space of the bubble and after 2.4 ps, the speed of the bubble jet was 30 times faster than before the shock wave passed through. These jet streamlines are focused toward the bubble center in the form of a high-speed jet.

The jet generated by bubble collapse is predicted to possess sufficient cavitation energy to cause intense physical stresses, followed by a crystal size reduction. The corresponding response of the solid electrolyte is shown in Figure 5(e), where the surface of the solid electrolyte is wrapped in a translucent yellow surface. The figure shows that the high-energy jet has a dramatic effect on the size reduction of the argyrodite materials. In the early state (5.0 ps), a cross-shaped pit is formed by the intense cavitation energy of the jet. Moreover, the dark blue region in Figure 5(b) indicates that a shockwave compression has occurred on the surface of the substance. The density of the solid electrolyte increased from 1.35 g/cm^3 to 1.90 g/cm^3.
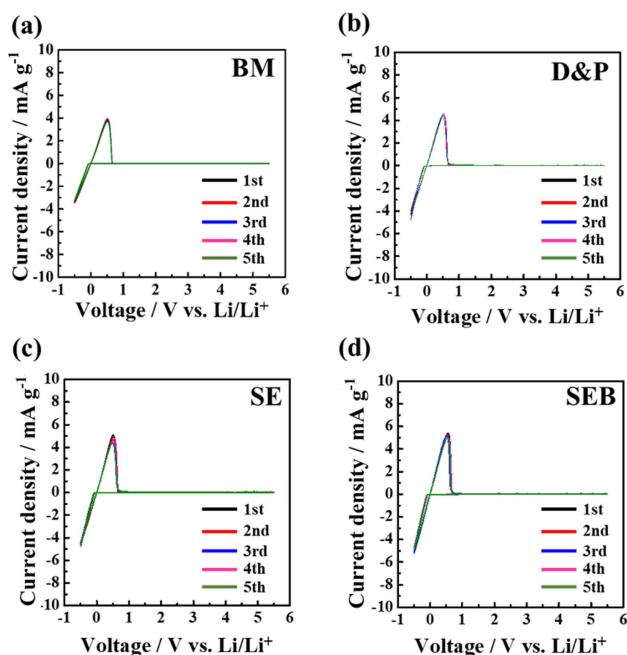
As time passed, this cross-shaped pit dug deeper and eventually split the solid electrolyte into several chunk-like pieces. However, the argyrodite structure of the small chunks was maintained even after separation by the jet. From these results, it is confirmed that the shock wave and jets generated during the bubble collapse process led to cavitation damage, resulting in particle reduction. This is in close agreement with the experimental observations of this study.

From the aforementioned results, it is considered that cavitation energy increases the local pressure in the vicinity of the crystal surface and consequently deforms the initial crystalline structure of the solid electrolyte. However, based only on these results, it is still unclear how much local pressure of cavitation energy is required to break the argyrodite structure. For a deeper understanding of these cavitation bubble collapse dynamics, the authors calculated the local pressure required for size reduction. For this, we adjusted the parameters that can affect the kinetic energy of the cavitation vortex, which is, the system temperature, shock intensity, size ratio between the solid electrolyte and bubble diameter, and offset distance between the bubble surface and nearest solid electrolyte surface. Comparing several cases, it was confirmed that the crystalline argyrodite structure was not broken when the local pressure of the cavitation energy was less than 6 MPa to 7 MPa. In these cases, size reduction of the solid electrolyte was not observed. However, when a cavitation energy of 80 MPa or more was transferred to the proximity of the surface, most of the lattice structures of the large solid electrolyte mass were shattered.

Evaluation of electrochemical performances

To compare the electrochemical stability of BM, D&P, SE, and SEB, a SUS|Li$_6$PS$_5$Cl solid electrolyte|Li–In cell was constructed (Figure 6), and the cyclic voltammograms (CV) of these cells were evaluated. The anodic and cathodic currents, which correspond to lithium dissolution (Li$\rightarrow$Li$^+$ + e$^-$) and lithium deposition (Li$^+$ + e$^-$ $\rightarrow$ Li), respectively, were confirmed to be ca. 0 V vs. Li/Li$^+$ in the voltammogram. There is no significant current due to electrolyte decomposition in the potential range from -0.5 to 5.5 V vs. Li/Li$^+$. The CV curves after the first cycle are almost identical to each other, demonstrating a good electrochemical reversibility against Li–In metal with an electrochemical window of more than 5.5 V. Furthermore, the current density of cells increases in the order of Li$_6$PS$_5$Cl prepared by SEB > SE > D&P > BM, meaning that the current density increases as the particle size of Li$_6$PS$_5$Cl decreases. In particular, in the case of SEB in Figure 6(d), the current density is higher than that in other cases, and the maintenance is good during five cycles because the particle distribution is uniformly small.

In Figure 7, we further investigated the performance of the Li$_6$PS$_5$Cl solid electrolyte for use in an all-solid-state cell consisting of commercial Li$_6$PS$_5$Cl as the separator membrane, NCM622 + Li$_6$PS$_5$Cl (fabricated by BM, D&P, SE, and SEB) + CNF as the composite cathode electrode, and Li–In alloy as the anode electrode. Using this solid electrolyte pellet, the torque

Batteries & Supercaps

Research Article
doi.org/10.1002/batt.202300036

Chemistry
Europe
European Chemical
Societies Publishing

Figure 6. CVs of Li_6PS_5Cl solid electrolytes in SUS│solid electrolyte│Li cells. The voltage window is between −0.5 and 5.5 V with a scan rate of 5 mV/s.

cell with the NCM622│Li_6PS_5Cl│CNF (60:35:5 in wt%) composite cathode and Li metal anode was compressed to 360 MPa for assembly. Figure 7(a) shows the top view and cross-sectional FE-SEM image of the composite positive electrode with Li_6PS_5Cl-mixed NCM powder after compression at 360 MPa. For the composite positive electrode layer with Li_6PS_5Cl prepared by BM mixed with NCM particles, voids were confirmed to exist between the Li_6PS_5Cl and NCM particles, and an intimate contact area between the membrane and electrode was not formed. The space around the NCM may not be filled due to the Li_6PS_5Cl particles being large, resulting in voids and a reduced contact area. Conversely, the composite cathode containing Li_6PS_5Cl fabricated by SEB was well-filled with Li_6PS_5Cl around the NCM, indicating that a favorable electrode-membrane interface was formed owing to the small size of the SEB particles.[65–67]

Figure 7(b) presents the charge-discharge curves of the cells, measured at a constant current density of 0.13 mA/cm² in the voltage range of ca. 2.4–3.7 V vs. Li–In. The cell with Li_6PS_5Cl prepared using the SEB-mixed NCM electrode exhibited a capacity of 176 mAh/g, which is the highest capacity compared to the analogous samples. This is because the contact area between the electrode and the membrane is increased by adding Li_6PS_5Cl prepared by SEB, which has a small particle size, into the electrode. The rate capability of a cell composed of a composite cathode mixed with Li_6PS_5Cl fabricated by SEB or BM is shown in Figure 7(c). The performance of the cell consisting of the composite cathode mixed with Li_6PS_5Cl fabricated by SEB was superior to that of the composite cathode mixed with Li_6PS_5Cl prepared by BM. This means that by using Li_6PS_5Cl prepared by the SEB method, a
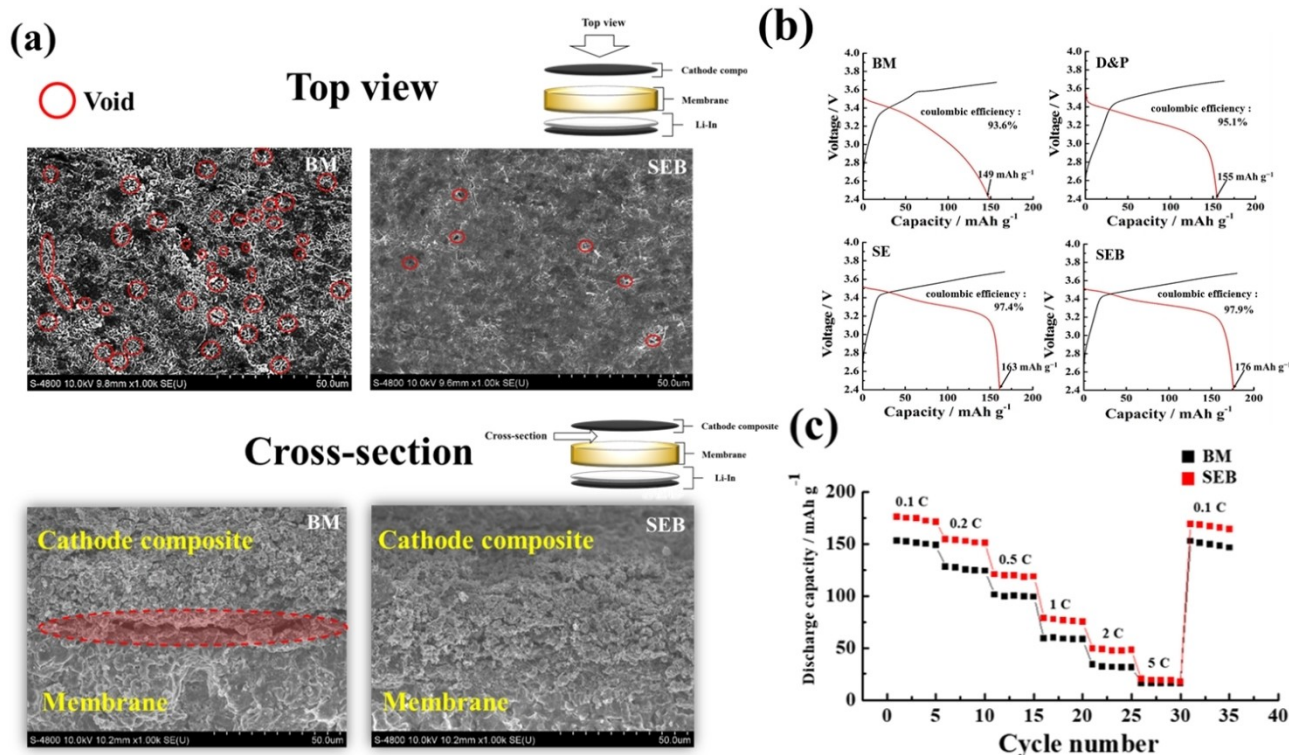
Figure 7. a) FE-SEM of NCM–Li_6PS_5Cl–CNF composite cathode. b) Charge-discharge profiles of NCM–Li_6PS_5Cl–CNF composite cathode│Li_6PS_5Cl solid electrolyte│Li metal anode cell at a C-rate of 0.1 C. c) Rate performance of 0.1 C, 0.2 C, 0.5 C, 1 C, 2 C, 5 C for the cell with the conventional mixed NMC electrode.

Batteries & Supercaps

Research Article
doi.org/10.1002/batt.202300036

Chemistry
Europe
European Chemical
Societies Publishing

solid electrolyte is well dispersed between the active materials and there is a dense and intimate interfacial contact at the electrolyte/electrode interfaces, so that the lithium ion conduction pathway can be made effectively. Remarkably, once the current rate returns to 0.1 C, the discharge capacity can recover to 168.2 mAh/g (95.5%), further suggesting the superior electrochemical reversibility of the cell. From these results, it is considered that the formation of a favorable interface between the active materials and the solid electrolyte is critical.

Conclusion

The sulfide-based solid electrolyte Li_6PS_5Cl was synthesized using a novel solution-processed synthesis method, which employs a solvent exchange process with a cavitation bubbling effect. In this pioneering SEB process, we exploited two solvents, the initial and final solvents, which have different boiling points and polarities. The initial solvent served to dissolve the solid electrolyte, and the final solvent served to independently precipitate the Li_6PS_5Cl particles from the solid electrolyte dissolved solution, preventing their agglomeration. Using this solvent exchange process, we synthesized a finer solid electrolyte than conventional methods, such as the BM or D&P methods. However, entangled particles between small primary particles were still observed, even with the SE method. To dissolve the agglomerations without unwanted side reactions, inert Ar gas bubbles were blown into the final solvent. It was confirmed that Li_6PS_5Cl prepared by this SEB method has the finest particle size of ca. 800 nm as well as a sufficient ionic conductivity of 1.54 mS cm^{-1} at 25 °C. Additionally, to clarify the detailed role and mechanism of the SEB bubbling process on the size reduction of Li_6PS_5Cl, MD simulations were performed. This showed that the high-energy jet generated by the collapse of the cavitation bubble induces significant physical stress and cleaves the large solid electrolyte mass into small argyrodite particles. In addition, it was confirmed that inducing the bubbling process with cavitation energies of 7 MPa to 80 MPa is suitable for synthesizing an appropriate argyrodite size reduction in the SEB method. In addition, the torque cell using this solid electrolyte pellet exhibited the highest capacity of 176 mAh/g and superior cell speed performance compared to cells with electrolytes manufactured by other processes due to the intimate contact area between the NCM electrode and Li_6PS_5Cl solid electrolyte. This result indicates

that our SEB method is a simple and effective protocol for producing size-controllable solid electrolytes that can maximize ASSLB cell performance. Therefore, we believe that this novel solution-processed synthesis can contribute to the development of all-solid-state technologies.

Experimental Section

Material synthesis and structural characterization

For direct morphological and electrochemical comparison of the Li_6PS_5Cl solid electrolyte synthesized by our novel SEB method and that synthesized by conventional methods, three samples were prepared using different synthesis methods: ball milling (BM), dissolution and precipitation (D&P), and solvent exchange (SE). Ball milling (BM) is a typical solid-state synthesis method, and commercial ball milling Li_6PS_5Cl (Jung-Kwan Co. Ltd., South Korea) powder was used in this paper. For the D&P method, wet synthetic Li_6PS_5Cl powder was prepared and synthesized. A Li_6PS_5Cl powder by BM was added to methanol and then stirred for 24 h at 25 °C. After stirring, a brown solid electrolyte solution was obtained. The solvent was then allowed to evaporate on a hot plate at 50 °C. The obtained brown powder was further dried overnight in an oven at 140 °C under vacuum to eliminate the remaining solvents. Finally, the dried powders were heat treated at 550 °C for 3 h in a quartz tube under Ar gas. All processes, except heat treatment, were conducted in an Ar-filled glove box (Korea Kiyon, dew point below −55 °C).

For the synthesis of the Li_6PS_5Cl solid electrolyte via the SE and SEB methods, a commercial solid-state synthesized Li_6PS_5Cl powder by BM was added to methanol and then stirred for 24 h at 25 °C. After stirring, the prepared solution (Li_6PS_5Cl + methanol) was dropped into heated toluene (90 °C) at a speed of 1.5 mL/s. A brown precipitate was obtained. The solvent was then allowed to evaporate on a hot plate at 90 °C. The obtained brown powder was further dried overnight in an oven at 140 °C under a vacuum to eliminate the remaining solvents. Finally, the dried powders were then heat-treated at 550 °C for 3 h under Ar flow in a quartz tube. During the entire synthesis process, there was a clear difference between the SE and SEB methods. For the novel SEB method, inert Ar gas for bubbling was injected into the final solvent during the solvent exchange a speed of 1.0 mL/min, as shown in Figure 1. The process, except for the Ar gas injection, was the same for both the SE and SEB methods. All processes, except heat treatment, were conducted in a glove box (Korea Kiyon, dew point at −0 °C).

X-ray diffraction (XRD) patterns were measured using an X-ray diffractometer (PANalytical X'pert Pro Powder Diffractometer) with an air-tightened holder. Diffraction data were collected in 0.01° steps from 10° to 80° in two sets. Field emission-scanning electron microscopy (FE-SEM, JSM-7619Plus, JEOL) images of the samples were obtained using a focused ion beam (FIB, 4 kV for 3 h, Ar ion beam) to prepare the samples for measurement.

Test cell fabrication and electrochemical measurements

The ionic conductivities of the samples were determined using alternating current impedance measurements. Prior to the impedance measurement, the samples were pelletized into polyether ether ketone (PEEK) mold and cylindrical type stainless disks 13 mm in diameter using a hydraulic press at 360 MPa. Indium foils (50 μm) on a stainless steel disk were used as the blocking electrodes and they were attached to both sides of the pellets. The AC impedance measurements were performed over a frequency range of 1 MHz–10 mHz at 25 °C using a Solartron 1260 impedance analyzer.

Cyclic voltammetry was conducted for SUS (stainless steel) | solid electrolyte | Li cells of Li6PS5Cl solid electrolytes with a voltage window of −0.5–5.5 V at a scan rate of 0.5 mV/s. Solid electrolyte layers were prepared by cold-pressing 0.20 g of solid electrolyte powder into a pellet under 360 MPa. For measuring the electro-

chemical performance, an all-solid-state cell (Li–In │ Li6PS5Cl solid electrolyte │ composite electrode powder). The composite electrode powder was prepared by hand mixing the NCM 622 (4 mm), Li6PS5Cl and CNF in a mortar for 30 minutes at a weight ratio of 60:35:5. Commercial solid-state-synthesized Li6PS5Cl (Jung-Kwan Co. Ltd., South Korea) powder was used as the separator. A cell (13 mm in diameter) cathode layer (15 mg), Li6PS5Cl solid electrolyte as a separator layer (150 mg), and Li–In alloy (diameter 13 mm, thickness 70 mm) were prepared by pressing at 360 MPa. The assembled half-cells were charged and discharged using a battery cycler (Won-A Tech.) In the potential range of 2.4–3.7 V (vs. Li–In) under 55 °C.

All test cells were applied with 4NM pressure by locking the bolt on the top of the jig before electrochemical measurement, and assembled in an argon glove box.

Computational simulation method

All molecular dynamics (MD) simulations were performed using the large-scale atomic/molecular massively parallel simulator (LAMMPS) package.[68] Post-processing and visualization were conducted using the open-source software Open Visualization Tool (OVITO).[69] Considering the computational resources available in the simulation computing clusters, the system contains 10^6 atoms with dimensions of $17 \times 17 \times 32$ nm^3 in the x, y, and z directions, respectively. To mimic the experimental conditions, a pure lithium argyrodite crystal (Li$_7$PS$_6$) consisting of $10 \times 10 \times 10$ unit cells with a lattice constant $a = 9.9926$ Å was suspended in a water solvent containing a similar-sized cavitation bubble (in diameter). The interaction among the atoms is described by a combination of force fields: TIP4P for water[70] and the 3-body Stillinger-Weber potential for Li$_7$PS$_6$.[71] The interaction between Li$_7$PS$_6$ and water was described by a combination of Lennard-Jones and electrostatic potentials with force-field parameters using the Lorentz-Berthelot combination rule.[72] The SHAKE algorithm was employed to constrain the O–H bond and H–O–H bond angles of the water molecules.[73]

The simulation was conducted as follows. First, energy minimization of the system was conducted using the conjugate gradient method. Subsequently, the cavitation bubble system was relaxed for 100 ps at 298 K with a time step of 1 fs using a canonical (NVT) ensemble with periodic boundary conditions along the x and y direction, and fixed boundary conditions along the z direction. During the relaxation, the bubble shape was well maintained, and the temperature and bulk water density converged to 0.98 g/cm^3 and 298 K, respectively. Finally, to study the process of bubble compression and collapse and the physicochemical size reduction mechanisms of argyrodite particles, shock waves were generated using a momentum mirror protocol applied previously in this type of simulation.[63,74,75] In this method, a piston moving with a velocity u_p impacts just outside the simulation box along the $+z$ direction. To prevent artificial conformations from overlapping the particles, a vacuum layer of 1 nm was added underneath the wall. The shock simulation was conducted in the microcanonical (NVE) ensemble with a 0.1 fs time step. In addition, free-boundary conditions were applied along the z direction. To mimic the propagation of shock pulses, the piston was stopped after a short time, and the formed shock wave was allowed to propagate with its motion in the $+z$ direction. Various simulation parameters, that is, bubbles of different diameters ($D = 3, 5, 7, 9$ nm), piston velocity ($u_p = 2, 2.5, 3.0, 3.5,$ and 4.0 km/s), piston stop times ($\tau_s = 1.25$ to 6.5 ps), and offset distance between the bubble surface and nearest solid electrolyte surface ($l = 1.5$ nm to 4 nm), were controlled to create shock waves and high-energy jets by bubble compression and collapse. Then, the shock wave propagates through the bubble, and the jet

streamline generated by the bubble collapse impacts the solid electrolyte surface with a greater force than the shock front. The total shock simulation time was greater than 75 ps, which was sufficient to observe these series of processes.

Acknowledgements

Conflict of Interest

The authors declare no conflict of interest.

Data Availability Statement

The data that support the findings of this study are available from the corresponding author upon reasonable request.

[1] J. B. Goodenough, Y. Kim, *Chem. Mater.* **2010**, *22*, 587–603.
[2] J.-M. Tarascon, *Philos. Trans. R. Soc. London Ser. A* **2010**, *368*, 3227–3241.
[3] N. Kamaya, K. Homma, Y. Yamakawa, M. Hirayama, R. Kanno, M. Yonemura, T. Kamiyama, Y. Kato, S. Hama, K. Kawamoto, *Nat. Mater.* **2011**, *10*, 682–686.
[4] K. H. Park, D. Y. Oh, Y. E. Choi, Y. J. Nam, L. Han, J. Kim, H. Xin, F. Lin, S. M. Oh, Y. S. Jung, *Adv. Mater.* **2016**, *28*, 1874–1883.
[5] A. Banerjee, K. H. Park, J. W. Heo, Y. J. Nam, C. K. Moon, S. M. Oh, S. Hong, Y. S. Jung, *Angew. Chem.* **2016**, *128*, 9786–9790; *Angew. Chem. Int. Ed.* **2016**, *55*, 9634–9638.
[6] R. Kanno, M. Murayama, *J. Electrochem. Soc.* **2001**, *148*, A742.
[7] R. Kanno, T. Hata, Y. Kawamoto, M. Irie, *Solid State Ionics* **2000**, *130*, 97–104.
[8] Y. Mo, S. P. Ong, G. Ceder, *Chem. Mater.* **2012**, *24*, 15–17.
[9] S. P. Ong, Y. Mo, W. D. Richards, L. Miara, H. S. Lee, G. Ceder, *Energy Environ. Sci.* **2013**, *6*, 148–156.
[10] P. Hartwig, W. Weppner, W. Wichelhaus, A. Rabenau, *Angew. Chem. Int. Ed.* **1980**, *19*, 74–75; *Angew. Chem.* **1980**, *92*, 72–73.
[11] W. Weppner, P. Hartwig, A. Rabenau, *J. Power Sources* **1981**, *6*, 251–259.
[12] K. Kitahama, Y. Furukawa, S. Kawai, O. Nakamura, *Solid State Ionics* **1981**, *3*, 335–339.
[13] P. Adeli, J. D. Bazak, K. H. Park, I. Kochetkov, A. Huq, G. R. Goward, L. F. Nazar, *Angew. Chem.* **2019**, *131*, 8773–8778; *Angew. Chem. Int. Ed.* **2019**, *58*, 8681–8686.
[14] X. Li, J. Liang, N. Chen, J. Luo, K. R. Adair, C. Wang, M. N. Banis, T. Sham, L. Zhang, S. Zhao, *Angew. Chem.* **2019**, *131*, 16579–16584; *Angew. Chem. Int. Ed.* **2019**, *58*, 16427–16432.
[15] T. Asano, A. Sakai, S. Ouchi, M. Sakaida, A. Miyazaki, S. Hasegawa, *Adv. Mater.* **2018**, *30*, 1803075.
[16] J. C. Bachman, S. Muy, A. Grimaud, H.-H. Chang, N. Pour, S. F. Lux, O. Paschos, F. Maglia, S. Lupart, P. Lamp, *Chem. Rev.* **2016**, *116*, 140–162.

[17] X. Yao, B. Huang, J. Yin, G. Peng, Z. Huang, C. Gao, D. Liu, X. Xu, *Chin. Phys. B* **2015**, *25*, 018802.

[18] J. W. Fergus, *J. Power Sources* **2010**, *195*, 4554–4569.

[19] D. Liu, W. Zhu, Z. Feng, A. Guerfi, A. Vijh, K. Zaghib, *Mater. Sci. Eng. B* **2016**, *213*, 169–176.

[20] M. A. Kraft, S. P. Culver, M. Calderon, F. Böcher, T. Krauskopf, A. Senyshyn, C. Dietrich, A. Zevalkink, J. Janek, W. G. Zeier, *J. Am. Chem. Soc.* **2017**, *139*, 10909–10918.

[21] C. Yu, S. Ganapathy, J. Hageman, L. van Eijck, E. R. H. van Eck, L. Zhang, T. Schwietert, S. Basak, E. M. Kelder, M. Wagemaker, *ACS Appl. Mater. Interfaces* **2018**, *10*, 33296–33306.

[22] Z. Zhang, L. Zhang, Y. Liu, C. Yu, X. Yan, B. Xu, L. Wang, *J. Alloys Compd.* **2018**, *747*, 227–235.

[23] S. Wang, Y. Zhang, X. Zhang, T. Liu, Y.-H. Lin, Y. Shen, L. Li, C.-W. Nan, *ACS Appl. Mater. Interfaces* **2018**, *10*, 42279–42285.

[24] S. Yubuchi, M. Uematsu, C. Hotehama, A. Sakuda, A. Hayashi, M. Tatsumisago, *J. Mater. Chem. A* **2019**, *7*, 558–566.

[25] S. Choi, J. Ann, J. Do, S. Lim, C. Park, D. Shin, *J. Electrochem. Soc.* **2018**, *166*, A5193.

[26] T. Inada, K. Takada, A. Kajiyama, M. Kouguchi, H. Sasaki, S. Kondo, M. Watanabe, M. Murayama, R. Kanno, *Solid State Ionics* **2003**, *158*, 275–280.

[27] H. Nakamura, T. Kawaguchi, T. Masuyama, A. Sakuda, T. Saito, K. Kuratani, S. Ohsaki, S. Watano, *J. Power Sources* **2020**, *448*, 227579.

[28] D. H. Kim, D. Y. Oh, K. H. Park, Y. E. Choi, Y. J. Nam, H. A. Lee, S.-M. Lee, Y. S. Jung, *Nano Lett.* **2017**, *17*, 3013–3020.

[29] R. P. Rao, S. Adams, *Phys. Status Solidi A* **2011**, *208*, 1804–1807.

[30] Y. Inoue, K. Suzuki, N. Matsui, M. Hirayama, R. Kanno, *J. Solid State Chem.* **2017**, *246*, 334–340.

[31] M. A. Kraft, S. Ohno, T. Zinkevich, R. Koerver, S. P. Culver, T. Fuchs, A. Senyshyn, S. Indris, B. J. Morgan, W. G. Zeier, *J. Am. Chem. Soc.* **2018**, *140*, 16330–16339.

[32] N. Minafra, S. P. Culver, T. Krauskopf, A. Senyshyn, W. G. Zeier, *J. Mater. Chem. A* **2018**, *6*, 645–651.

[33] L. Zhou, K.-H. Park, X. Sun, F. Lalère, T. Adermann, P. Hartmann, L. F. Nazar, *ACS Energy Lett.* **2018**, *4*, 265–270.

[34] T. Shi, Q. Tu, Y. Tian, Y. Xiao, L. J. Miara, O. Kononova, G. Ceder, *Adv. Energy Mater.* **2020**, *10*, 1902881.

[35] S. Boulineau, M. Courty, J.-M. Tarascon, V. Viallet, *Solid State Ionics* **2012**, *221*, 1–5.

[36] C. Yu, L. van Eijck, S. Ganapathy, M. Wagemaker, *Electrochim. Acta* **2016**, *215*, 93–99.

[37] D. A. Ziolkowska, W. Arnold, T. Druffel, M. Sunkara, H. Wang, *ACS Appl. Mater. Interfaces* **2019**, *11*, 6015–6021.

[38] S. Chida, A. Miura, N. C. Rosero-Navarro, M. Higuchi, N. H. H. Phuc, H. Muto, A. Matsuda, K. Tadanaga, *Ceram. Int.* **2018**, *44*, 742–746.

[39] Z. Zhang, L. Zhang, Y. Liu, X. Yan, B. Xu, L. Wang, *J. Alloys Compd.* **2020**, *812*, 152103.

[40] M. Ghidiu, J. Ruhl, S. P. Culver, W. G. Zeier, *J. Mater. Chem. A* **2019**, *7*, 17735–17753.

[41] M.-J. Kim, J.-W. Park, B. G. Kim, Y.-J. Lee, Y.-C. Ha, S.-M. Lee, K.-J. Baeg, *Sci. Rep.* **2020**, *10*, 1–11.

[42] M.-S. Kim, H.-S. Song, H. J. Park, S.-J. Hwang, *Chem. Pharm. Bull.* **2012**, *60*, 543–547.

[43] N. T. K. Thanh, N. Maclean, S. Mahiddine, *Chem. Rev.* **2014**, *114*, 7610–7630.

[44] T. Shi, Q. Tu, Y. Tian, Y. Xiao, L. J. Miara, O. Kononova, G. Ceder, *Adv. Energy Mater.* **2020**, *10*, 1902881.

[45] D. Zhou, A. A. Keller, *Water Res.* **2010**, *44*, 2948–2956.

[46] M. H. Hussain, N. F. Abu Bakar, A. N. Mustapa, K.-F. Low, N. H. Othman, F. Adam, *Nanoscale Res. Lett.* **2020**, *15*, 1–10.

[47] H. Zhang, B. Chen, J. F. Banfield, *J. Phys. Chem. C* **2010**, *114*, 14876–14884.

[48] X. Wang, Y. Zhang, X. Zhang, T. Liu, Y.-H. Lin, L. Li, Y. Shen, C.-W. Nan, *ACS Appl. Mater. Interfaces* **2018**, *10*, 24791–24798.

[49] S. Sumari, A. Roesyadi, S. Sumarno, *St. Cerc. St. CICBIA.* **2013**, *14*, 229.

[50] A. Kollath, N. Brezhneva, E. v Skorb, D. v Andreeva, *Phys. Chem. Chem. Phys.* **2017**, *19*, 6286–6291.

[51] N. H. H. Phuc, K. Morikawa, T. Mitsuhiro, H. Muto, A. Matsuda, *Ionics* **2017**, *23*, 2061–2067.

[52] H. Deiseroth, S. Kong, H. Eckert, J. Vannahme, C. Reiner, T. Zaiß, M. Schlosser, *Angew. Chem. Int. Ed.* **2008**, *47*, 755–758; *Angew. Chem.* **2008**, *120*, 767–770.

[53] S. Ito, M. Nakakita, Y. Aihara, T. Uehara, N. Machida, *J. Power Sources* **2014**, *271*, 342–345.

[54] B. Davaasuren, F. Tietz, *Solid State Ionics* **2019**, *338*, 144–152.

[55] F. Strauss, J. Lin, J. Janek, T. Brezesinski, *Sci. Rep.* **2021**, *11*, 1–9.

[56] M. Eom, J. Kim, S. Noh, D. Shin, *J. Power Sources* **2015**, *284*, 44–48.

[57] J. S. Park, L. Cheng, V. Zorba, A. Mehta, J. Cabana, G. Chen, M. M. Doeff, T. J. Richardson, J. H. Park, J.-W. Son, *Thin Solid Films* **2015**, *576*, 55–60.

[58] S. Wang, W. Zhang, X. Chen, D. Das, R. Ruess, A. Gautam, F. Walther, S. Ohno, R. Koerver, Q. Zhang, *Adv. Energy Mater.* **2021**, *11*, 2100654.

[59] Y. Wang, D. Lu, M. Bowden, P. Z. el Khoury, K. S. Han, Z. D. Deng, J. Xiao, J.-G. Zhang, J. Liu, *Chem. Mater.* **2018**, *30*, 990–997.

[60] J. Maier, *Mater. Sustain. Energy* **2011**, 160–170.

[61] A. R. Symington, M. Molinari, J. A. Dawson, J. M. Statham, J. Purton, P. Canepa, S. C. Parker, *J. Mater. Chem. A* **2021**, *9*, 6487–6498.

[62] Y.-T. Wu, A. Adnan, *Sci. Rep.* **2017**, *7*, 1–9.

[63] S. Zhan, H. Duan, L. Pan, J. Tu, D. Jia, T. Yang, J. Li, *Phys. Chem. Chem. Phys.* **2021**, *23*, 8446–8455.

[64] S. T. Kong, Ö. Gün, B. Koch, H. J. Deiseroth, H. Eckert, C. Reiner, *Chem. Eur. J.* **2010**, *16*, 5138–5147.

[65] C. Yu, S. Ganapathy, N. J. J. de Klerk, I. Roslon, E. R. H. van Eck, A. P. M. Kentgens, M. Wagemaker, *J. Am. Chem. Soc.* **2016**, *138*, 11192–11201.

[66] J. Auvergniot, A. Cassel, J.-B. Ledeuil, V. Viallet, V. Seznec, R. Dedryvère, *Chem. Mater.* **2017**, *29*, 3883–3890.

[67] A. Banerjee, X. Wang, C. Fang, E. A. Wu, Y. S. Meng, *Chem. Rev.* **2020**, *120*, 6878–6933.

[68] S. Plimpton, *J. Comput. Phys.* **1995**, *117*, 1–19.

[69] A. Stukowski, *Model Simul. Mater. Sci. Eng.* **2010**, *18*, 15012.

[70] J. L. F. Abascal, C. Vega, *J. Chem. Phys.* **2005**, *123*, 234505.

[71] S. Ariga, T. Ohkubo, S. Urata, Y. Imamura, T. Taniguchi, *Phys. Chem. Chem. Phys.* **2022**, *24*, 2567–2581.

[72] H. A. Lorentz, *Ann. Phys.* **1881**, *248*, 127–136.

[73] H. C. Andersen, *J. Comput. Phys.* **1983**, *52*, 24–34.

[74] G. Zhou, P. Rajak, S. Susarla, P. M. Ajayan, R. K. Kalia, A. Nakano, P. Vashishta, *Sci. Rep.* **2018**, *8*, 1–9.

[75] K. Nomura, R. K. Kalia, A. Nakano, P. Vashishta, *Appl. Phys. Lett.* **2007**, *91*, 183109.